Supplemental Document

OPTICA

# Dose-efficient *in vivo* X-ray phase contrast imaging at micrometer resolution by Bragg magnifiers: supplement

REBECCA SPIECKER,[1,*] PAULINE PFEIFFER,[2] ADYASHA BISWAL,[3,4] MYKOLA SHCHERBININ,[1] MARTIN SPIECKER,[5] HOLGER HESSDORFER,[3] MATHIAS HURST,[3] YAROSLAV ZHAROV,[1] VALERIO BELLUCCI,[1,6] TOMÁŠ FARAGÓ,[3] MARCUS ZUBER,[3] ANNETTE HERZ,[7] ANGELICA CECILIA,[3] MATEUSZ CZYZYCKI,[1] CARLOS SATO BARALDI DIAS,[3] DMITRI NOVIKOV,[8] LARS KROGMANN,[2] ELIAS HAMANN,[3] THOMAS VAN DE KAMP,[1,3] AND TILO BAUMBACH[1,3]

[1]*Laboratory for Applications of Synchrotron Radiation (LAS), Karlsruhe Institute of Technology (KIT), Kaiserstr. 12, Karlsruhe, 76131, Germany*
[2]*Department of Entomology, State Museum of Natural History, Rosenstein 1, Stuttgart, 70191, Germany*
[3]*Institute for Photon Science and Synchrotron Radiation (IPS), Karlsruhe Institute of Technology (KIT), Hermann-von-Helmholtz-Platz 1, Eggenstein-Leopoldshafen, 76344, Germany*
[4]*Centre for Organismal Studies, Heidelberg University, Im Neuenheimer Feld 230, Heidelberg, 69120, Germany*
[5]*Physikalisches Institut, Karlsruhe Institute of Technology (KIT), Kaiserstr. 12, Karlsruhe, 76131, Germany*
[6]*European X-Ray Free-Electron Laser Facility GmbH, Holzkoppel 4, Schenefeld, 22869, Germany*
[7]*Julius Kühn-Institute, Institute for Biological Control, Schwabenheimer Str. 101, Dossenheim, 69221, Germany*
[8]*Deutsches Elektronen-Synchrotron DESY, Notkestr. 85, Hamburg, 22607, Germany*
[*]*rebecca.spiecker@kit.edu*



Supplement DOI: https://doi.org/10.6084/m9.figshare.24347491

Parent Article DOI: https://doi.org/10.1364/OPTICA.500978

# Dose-efficient *in vivo* X-ray phase contrast imaging at micrometer resolution by Bragg magnifiers: supplemental document

## 1. MATERIALS AND METHODS

**Bragg magnifier setup and characterization measurements** The Si crystals (*Crystal Scientific (UK) Ltd, Alnwick, United Kingdom*) have dimensions of 21 cm x 8 cm x 2 cm and an asymmetry angle specified to be 5.92(2)°, yielding a physical input field of view (FOV) of 0.3 mm x 0.3 mm to 1.5 mm x 1.5 mm, depending on the magnification, and an output FOV of 45 mm x 45 mm. Each crystal is precisely aligned with respect to the synchrotron X-ray beam using a high-precision hexapod (*Physik Instrumente (PI) GmbH & Co. KG, 76228 Karlsruhe, Germany*). The Lambda SPCD (*X-Spectrum GmbH, 22547 Hamburg, Germany*) has a GaAs sensor of 500 µm thickness bonded to a 6 x 2 Medipix3RX chip array with a pixel size of 55 µm [1], operated in single-pixel mode at 6 keV threshold. We expect that the efficiency of the BM system would even further benefit by measuring in charge-summing mode for suitable photon fluxes. Fig. S1E shows a photograph of the setup. The reflectivity of a single Si crystal was measured to be 96.5(6) % (theoretical value: 97.4 %). The asymmetry angles were determined experimentally to be 5.928(8)° and 5.916(9)°. The small deviations cause a slight difference in the magnification factor in the horizontal and vertical direction. This can also be found from a detailed analysis of the data shown in Fig. 2E, where the magnifications are $M_x = 26.5$ and $M_y = 26.0$ (theoretical: $M = 26.3$) as well as $M_x = 171$ and $M_y = 160$ (theoretical: $M = 163$) at 29.05 keV and 31.07 keV, respectively. Horizontal and vertical propagation distances were $z_x = 0.22$ m and $z_y = 0.60$ m. For the resolution measurement at 31 keV, holograms of a test pattern (*model X500-200-16, Carl Zeiss Microscopy GmbH, 07745 Jena, Germany*) were acquired at ten propagation distances with $z_x = 0.15$–$0.41$ m and $z_y = 0.53$–$0.79$ m. Multidistance phase reconstruction was performed with the *HoloTomoToolbox* [2]. The parameters used for the reconstruction are a ratio of $\beta/\delta = 10^{-1.33}$ (gold), where $\beta$ is the imaginary part of the refractive index, and regularization parameters of $\alpha_{\text{low-freq}} = 0$ and $\alpha_{\text{high-freq}} = 10^{-1}$ for low and high spatial frequencies, respectively. The different horizontal and vertical propagation distances were taken into account [3], which is facilitated by the *HoloTomoToolbox*. Using the 220 reflection of Ge crystals with $\alpha = 5.66°$, the resolution can be further increased by a factor of 2 due to their larger Darwin width at the expense of a decreased total reflectivity to nominally 63 %, see also Fig. S1C.

**Indirect detector system** The indirect detector system consists of a 12 µm thick LSO:Tb scintillator [4], a diffraction-limited optical microscope (*Optique Peter, 69210 Lentilly, France*, 10x objective lens with numerical aperture of 0.28, *model 378-803-3, Mitutoyo Deutschland GmbH, 41469 Neuss, Germany*, and 180 mm tubus lens resulting in 9x total magnification [5]), and a pco.edge 5.5 CMOS camera (*PCO AG, 93309 Kelheim, Germany*) with a physical pixel size of 6.5 µm x 6.5 µm, yielding an effective pixel size of 0.72 µm. The pco.edge camera shows a readout noise of 3 counts (root-mean-square) per pixel. This corresponds to $\sim$ 4 X-ray photons incident on the indirect system, meaning that for more than $\sim$ 16 incident X-ray photons per pixel the photon shot noise is the dominant noise source.

**Experimental comparison between the BM and the indirect system** Comparing the imaging performance of the BM system with the indirect system (Fig. 3), images of a Siemens star (Fig. 3A and Fig. S2) were acquired at ten propagation distances with $z = 0.15$–$0.41$ m for the indirect system and $z_x = 0.15$–$0.41$ m and $z_y = 0.53$–$0.79$ m for the BM system. The energy was set to 30.5 keV so that the effective pixel sizes of the BM system (0.72 µm horizontally and 0.66 µm vertically) are similar to the indirect system. First, the images were acquired at the same X-ray fluence ($6 \cdot 10^3$ ph/µm$^2$ per frame), then the flux for the indirect system was increased by a factor of $\sim$ 7 to compensate for its lower detection efficiency. The X-ray fluence was determined using

the SPCD. Unfortunately, at four propagation distances, the test pattern slightly moved out of the FOV of the BM. Therefore, we decided to complete the data of the missing pixel rows by duplicating the corresponding pixel rows from the opposite side of the image (4 % of the overall data set). For details, see the publicly available data. For the phase reconstruction, raw images acquired with the BM system were flatfield-corrected. Raw images of the indirect system were flat- and darkfield-corrected. In all images, hot pixels were removed by interpolation. Multidistance phase reconstruction was performed with the *HoloTomoToolbox* [2], again with $\beta/\delta = 10^{-1.33}$, $\alpha_{\text{low-freq}} = 0$, and $\alpha_{\text{high-freq}} = 10^{-1}$. For the images shown in Fig. 3D, the incident beam was attenuated by a factor of about 400 to 200 ph/µm$^2$ and the exposure time was 67 ms. Propagation distances were $z = 0.22$ cm for the indirect detector and $z_x = 0.22$ m and $z_y = 0.60$ m for the BM system, and the tomograms were acquired with 1000 projections each. For automated data acquisition, we used the control system *Concert* [6], and for the tomogram, data pre-processing, Paganin phase retrieval [7] (again adapted to the different horizontal and vertical propagation distances for the BM [3], and visually adjusting $\beta/\delta$ to $10^{-1.7}$ for the dried insect sample), and tomographic reconstruction with filtered back-projection was performed with the *tofu* framework [8].

**Study specimens** Eggs of the Angoumois grain moth (*Sitotroga cerealella* (Lepidoptera: Gelechiidae)) parasitized by *Trichogramma cacoeciae* (Hymenoptera: Chalcidoidea: Trichogrammatidae) were obtained from Julius Kühn-Institute. Host eggs with parasitoids inside were incubated at 25 °C, 70 % relative humidity, under long-day conditions (16 h light: 8 h dark) until just before hatching and then brought to room temperature. As *Trichogamma cacoeciae* is a thelytokous species, all wasps are female.

**Data acquisition and image processing for *in vivo* measurements** The tomogram of a *Trichogramma* wasp inside its host egg shown in Fig. 4A was acquired *in vivo* with 1000 projections and the same imaging parameters as for Fig. 4B-F and Mov. S2 (see below), resulting in an estimated total dose of $\sim 7$ Gy. The amount of projections could be further reduced, e.g., using algebraic reconstruction or neural networks [9, 10]. Also here, data pre-processing, phase retrieval [7], and tomographic reconstruction was performed with the *tofu* framework [8], and the rendering was done using *Drishti* [11]. For the radiographic *in vivo* measurements of *Trichogramma* wasps inside their host eggs, the specimens were selected with a light optical microscope and scanned individually in Eppendorf tubes. Since it is not possible to predict the time of emergence from the outside, we used a dark discoloration of the egg shell as indication whether the wasp will soon start to emerge. In total, 68 samples were chosen, from which six emerged during the observation under radiation and three datasets of the full emergence process were acquired. The observation was performed intermitted by radiation-free pauses to reduce the overall dose and to catch the emergence phase. The total exposure time to X-rays of the emerging wasps varied between 15–72 min with a total observation time of up to 2 h. The data shown in Fig. 4B-D were acquired at 100 ph/µm$^2$/frame, an image repetition rate of 15 Hz, propagation distances of $z_x = 22$ cm and $z_y = 60$ cm, and a photon energy of 30.4 keV. At this energy, the spatial resolution is 1.7 µm, the magnification is 64-fold and the complete insect fits into the FOV of 0.6 mm x 0.4 mm. The FOV is limited vertically by the size of the SPCD and horizontally by the length of the crystal. The dose per frame is $\sim 7$ mGy, and the total dose for Mov. S2 is $\sim 200$ Gy. For the observation of mandible movement (Fig. 4E, F), Ge crystals were used at 30.5 keV and $\sim 1000$ ph/µm$^2$/frame with 15 Hz image repetition rate and a total dose of 90 Gy for Mov. S3. To exploit the full information contained in the recorded image up to the resolution limit, phase retrieval for all *in vivo* radiographic measurements was performed based on Tikhonov regularization (NLTikh) [12] using the *HoloTomoToolbox* [2] ($\beta/\delta = 10^{-2.5}$, $\alpha_{\text{low-freq}} = 10^{-4.5}$, $\alpha_{\text{high-freq}} = 10^{-1}$) and again taking the different horizontal and vertical propagation distances into account [3].

## 2. CALCULATION OF OPTIMAL OPERATING ENERGIES FOR PHASE CONTRAST IMAGING

In the main text, we discuss at which energy the highest SNR per dose can theoretically be achieved for PB-PCI and soft tissue. Here, we explain how the curves in Fig. 1A, B are calculated. The dose $D$ is defined as the total energy $E_{\text{abs}}^{\text{tot}}$ deposited in the sample per mass $m = \rho d A$, where $\rho$ is the sample density, $d$ the sample thickness along the X-ray path, and $A$ the irradiated area on the sample. Using the Lambert-Beer law with the linear attenuation coefficient $\mu$, the amount of X-ray photons per unit area absorbed or scattered by the sample is given by [13]

$$n_{\text{abs}} = n_0 - n_{\text{tr}} = n_0 \cdot (1 - e^{-\mu d}), \tag{S1}$$

where $n_0$ is the amount of incident photons per unit area, i.e., the photon fluence, and $n_{\text{tr}}$ the amount of photons transmitted through the sample. During the interaction process, in average only a fraction of the primary X-ray photon energy $E$ is transferred to the sample, which is described by the energy absorption coefficient $\mu_{\text{en}}$. The mean absorbed energy per interacting photon is

$$E_{\text{abs}} = \frac{\mu_{\text{en}}}{\mu} \cdot E.$$

Thus, the dose deposited in the sample is given by [13]

$$D = \frac{E_{\text{abs}}^{\text{tot}}}{m} = \frac{\mu_{\text{en}}}{\mu} \frac{E}{\rho d A} \cdot n_{\text{abs}} \cdot A = \frac{\mu_{\text{en}}}{\mu} \frac{E}{\rho d} n_0 \cdot (1 - e^{-\mu d}). \tag{S2}$$

Here, we assume that the probability to undergo an interaction process is low, such that multiple scattering can be neglected. This assumption was verified by simulations for $d = 1\,\text{mm}$ using the software toolkit *Geant4* [14], taking into account multiple scattering. For $\mu d < 1$, i.e., high energies or thin samples, Eq. S2 can be linearized and results in

$$D = \frac{\mu_{\text{en}}}{\rho} \cdot E \cdot n_0.$$

For low energies ($E < 20\,\text{keV}$), where photoelectric absorption is the dominant interaction process and where contribution from Compton scattering can be neglected, one finds $\mu_{\text{en}} \approx \mu \propto E^{-x}$ with $x \approx 3$. Consequently, $D \propto E^{-2}$ at low energies. In Fig. 1A in the main text, we show that the dose curve at constant incident photon fluence flattens out for $E > 20\,\text{keV}$ due to Compton scattering and reaches a minimum at 60 keV.

With increasing $E$, the phase shift imposed to X-rays when traversing a medium decreases as well. The phase shift $\phi$ is proportional to $\delta \cdot E$, where $1 - \delta$ is the real part of the complex index of refraction [15]. Far from atomic resonances, it holds

$$\delta = \frac{r_e \lambda^2 n_e}{2\pi} = \frac{r_e h^2 c^2 n_e^w}{2\pi} \underbrace{\frac{n_e}{n_e^w \rho}}_{\eta} \cdot \frac{\rho}{E^2} \propto \frac{\eta \rho}{E^2},$$

where $r_e$ is the classical electron radius, $n_e$ the electron density, $\lambda$ the X-ray wavelength, $h$ the Planck constant and $c$ the speed of light. Here, we introduce the electron density $n_e^w$ of water as reference value and express $n_e$ via $\rho$ and a material-dependent quantity $\eta$, which is approximately constant [16]. A measure for the image quality and dose efficiency is the SNR. For PB-PCI and weak phase objects, the signal $S$ in the image is proportional to the phase, and thus $S \propto \phi \propto \eta \rho E^{-1}$. In total, we obtain the dependency

$$\text{SNR} \propto \frac{n_{\text{tr}} A_{\text{px}} \cdot \phi}{\sqrt{n_{\text{tr}} A_{\text{px}}}} \propto \sqrt{n_{\text{tr}} A_{\text{px}}} \cdot \eta \rho E^{-1} = \eta \rho^{3/2} \sqrt{\frac{\mu}{\mu_{\text{en}}} \frac{D d A_{\text{px}}}{E^3} \frac{1}{e^{\mu d} - 1}}, \tag{S3}$$

where $A_{\text{px}}$ is the pixel size of the detector. This equation was used to generate Fig. 1B in the main text. In order to gain a better understanding for the energy regime where photoelectric absorption is dominant (see above), we rewrite Eq. S3 and obtain

$$\text{SNR} \propto \eta \rho^{3/2} \sqrt{\frac{D A_{\text{px}}}{1 + \frac{\mu d}{2} + \frac{(\mu d)^2}{6} + \dots}}.$$

Here, we see the relevant dependencies of the SNR in this energy regime. For a given dose, the SNR becomes constant in energy when the X-ray energy is high enough ($\mu d < 1$) so that most of the incident photons pass the sample. For even higher energies where Compton scattering comes into play, the SNR decreases (see Fig. 1B in the main text).

## 3. EXPERIMENTAL EVALUATION OF GAIN IN DQE

In the following, we describe in more detail the experimental evaluation of the gain $G(q)$ in DQE of the BM compared to the indirect system over spatial frequency $q$ shown in the main text in Fig. 3C. Following Eq. 1 in the main text, we determine $G(q)$ by evaluating $\mathrm{SNR}^2(q)$ of both systems at the same dose and energy (Fig. 3B). For ten propagation distances, we record at each distance in quick succession 50 sample images of a Siemens star test pattern as well as 50 flatfield images. For precise determination of the noise, we subtract two subsequent flatfield images to eliminate inhomogeneities in the flatfields. The resulting additional factor of $\sqrt{2}$ in the noise (Gaussian error propagation) is taken into account for the further evaluation. From the resulting 25 images, we compute the Fourier transform and obtain the noise $N(q_x, q_y)$ by determining the standard deviation of the 25 images for each $q_x, q_y$. For the indirect system, $N$ is corrected for the readout noise of the camera, extracted from 50 darkfield images (without X-ray illumination). We subtract the flatfields from the sample images at each propagation distance to remove inhomogeneities. For phase contrast imaging, strictly speaking neither division [17] nor subtraction provides perfect correction. Since we find that for our case subtraction works equally well as division for the removal of inhomogeneities, we decided to use subtraction here due to the simpler error propagation. We determine the complex measured signal $S_\mathrm{m}(q_x, q_y)$ in Fourier space by averaging over all 50 sample images. Note that due to the averaging, $S_\mathrm{m}$ can be determined below the noise floor of a single image. To be precise, the variance of the averaged measured signal is $N^2/25$. The spectral density $S^2$ of the signal $S(q_x, q_y)$ can then be determined by $S^2 = S_\mathrm{m}^2 - N^2/25$. Next, we compute the azimuthal average of the energy density $S^2(q)$ and squared noise $N^2(q)$ emitted into spatial frequencies with radius $q$. Finally, we obtain $\mathrm{SNR}^2(q) = S^2(q)/N^2(q)$ for each propagation distance. The procedure has been verified on artificial data. In Fig. 3B, we averaged the $\mathrm{SNR}(q)$ over all ten propagation distances.

As mentioned in the main text, the BM system has a larger propagation distance in vertical direction. Here, we want to compare both systems independently of the free space contrast transfer function [15]. For the calculation of the DQE ratio, we therefore perform a small correction by simulating holograms of the Siemens star test pattern for both imaging systems and for each propagation distance. Using the measured incident photon fluence, we simulate 50 sample and 50 flatfield images and follow the procedure as described for the measured data above in order to obtain the ideal input $\mathrm{SNR}^2_{\mathrm{BM,sim}}$ and $\mathrm{SNR}^2_{\mathrm{ind,sim}}$. For the sake of clarity, we omit the index 0 in the notation of the input $\mathrm{SNR}_0$. The simulation was performed for the ideal case of no source blur and an ideal $\mathrm{OTF}(q) = 1$. We create the sample numerically and simulate the propagated image intensity using the full free space propagator for the indirect system [15] and the shift-variant propagator based on Refs. [3, 18] for the BM system, though shift-variance does not have a visible effect here. We include oversampling, padding, and then binning and cropping to prevent aliasing. The simulation takes into account the different horizontal and vertical propagation distances $z_x$ and $z_y$ of the BM system and the slightly different magnifications $M_x$ and $M_y$ as well as the slight discrepancy in the pixel areas of both systems. Note that for clarity in Fig. 3B in the main text, we show only the simulated SNR for the propagation distances of the BM system. The simulated SNR curves for both systems are shown in Fig. S2. The gain in DQE is given by

$$G(q) = \frac{\mathrm{SNR}^2_{\mathrm{BM}}(q)}{\mathrm{SNR}^2_{\mathrm{ind}}(q)} \cdot \frac{\mathrm{SNR}^2_{\mathrm{ind,sim}}(q)}{\mathrm{SNR}^2_{\mathrm{BM,sim}}(q)},$$

where $\mathrm{SNR}^2_{\mathrm{BM}}$ and $\mathrm{SNR}^2_{\mathrm{ind}}$ are extracted from the experimental data of the BM or indirect system, respectively. The correction $\mathrm{SNR}^2_{\mathrm{ind,sim}}(q)/\mathrm{SNR}^2_{\mathrm{BM,sim}}(q)$ reduces the spread in $G(q)$ (green points in Fig. 3C in the main text).

## 4. DETAILS ON THE BRAGG MAGNIFIER SYSTEM

In Fig. S1, we show further details on the crystal properties and the experimental setup. For our setup with Si crystals, an asymmetry angle of $\alpha = 5.92°$ was chosen in order to reach best possible spatial resolution at 31 keV by maximizing the angular crystal acceptance (Darwin width, see Fig. S1A). The Darwin width and thus the resolution limit vary with energy (Fig. S1B). Further, the Darwin width of the asymmetric 220 reflection is considerably enlarged compared to the Darwin width of the preceding symmetrically diffracting Si [111] double-crystal monochromator. Exchanging the Si crystals by Ge crystals leads to improved spatial resolution at the expense of lower reflectivity and thus lower efficiency (see Fig. S1C). The Ge 220 reflectivity curves have approximately twice the Darwin widths of the corresponding Si 220 curves (Fig. S1C), i.e. an attainable resolution of 0.6 µm as defined by Eq. 3 in the main text.
In the experiment (Fig. S1D, E), the first crystal magnifies the image in horizontal direction and the second crystal in vertical direction. This configuration was chosen since the source from the third generation synchrotron is smaller vertically and causes less source blur in this direction, allowing for longer vertical propagation distances.

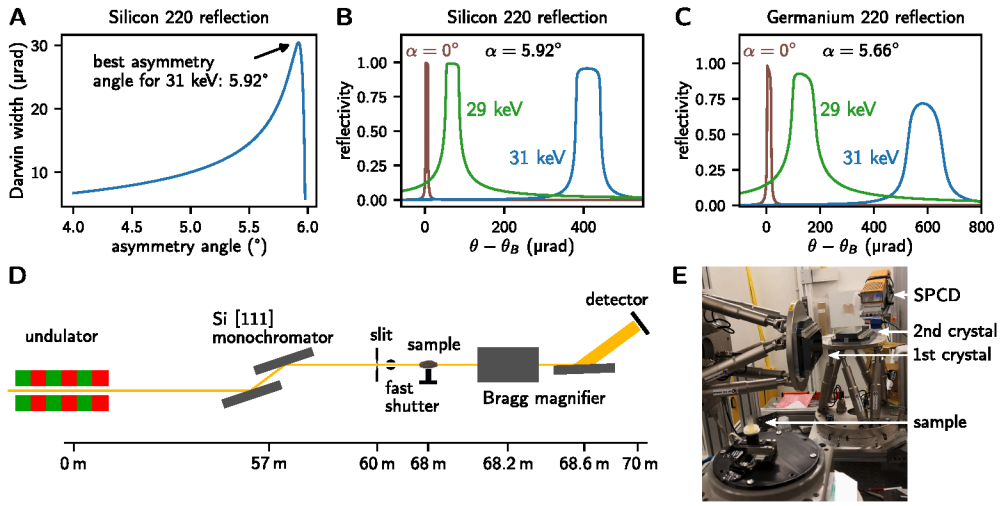


**Fig. S1.** Details on the Bragg magnifier system. **A** Darwin width of a Si 220 reflection at different asymmetry angles for an energy of 31 keV, taking into account dynamical diffraction with a strongly asymmetric diffraction geometry [19]. **B** Simulated reflectivity curves [19] of the Si 220 reflection for the symmetric case and for an asymmetry angle of 5.92°. **C** The 220 reflection of Ge crystals with an asymmetry angle of $\alpha = 5.66°$ can be used as well. Note the different scale on the horizontal axis. **D** Sketch of the beamline and experimental layout used for the experiment. **E** Photograph of the BM setup installed at the P23 beamline, PETRA III, DESY, Hamburg. Both crystals are mounted on a hexapod for flexible alignment. The beam passes through the sample, is magnified by the crystals in two dimensions and detected with a Lambda GaAs SPCD.

## 5. ADDITIONAL INFORMATION ON THE DETECTOR COMPARISON

### A. Siemens star measurements

For the experimental comparison, we recorded propagation-based phase contrast holograms of a Siemens star test pattern at ten propagation distances. Fig. S2 shows an extended version of the experimental data depicted in Fig. 3A in the main text. The corresponding simulations of the input wavefield were performed for perfect coherence and an ideal $\mathrm{OTF}(q) = 1$, i.e., excluding influence by the BM crystals or the magnifying optics of the indirect system. Examples of the simulations are shown in the first column of Fig. S2, and the resulting simulated and averaged SNR for both systems is given as well. These curves were used for the experimental evaluation in Fig. 3C in the main text. The different horizontal and vertical propagation distances for the BM system were taken into account in the simulations [3]. The images with the indirect system were first acquired at the same photon intensity as the images with the BM and second at seven times higher flux to compensate approximately for the lower X-ray detection efficiency of the indirect system. Even for the increased intensity (third row), the contrast in the indirect system is strongly suppressed compared to both the simulation and the experimental images of the BM system. As discussed in the main text, this can be attributed to the OTF of the indirect system, which increasingly suppresses the contrast transfer with increasing spatial frequencies $q$. The image distortion by the OTF as well as by source blur can partially be removed by deconvolution [20–25]. For the BM system, the OTF is close to unity until the resolution limit, which is why no OTF correction is needed. The reconstructed values correspond to the expected phase shift of −0.8 rad (1.4 µm gold layer). For the indirect system, source blur can be neglected in comparison to the OTF of the microscope (cf. experimental $\mathrm{SNR_{BM}}$ vs. $\mathrm{SNR_{ind}}$ in Fig. 3B). Neglecting minor aberrations by the finite thickness of the scintillator, we use the incoherent OTF of an ideal lens, given by

$$\mathrm{OTF}(\nu) = \frac{2}{\pi}\left(\arccos|\nu| - |\nu|\sqrt{1-\nu^2}\right)$$

with $\nu = q/q_{\mathrm{max}}$ and $q_{\mathrm{max}} = 2\mathrm{NA}/\lambda_{\mathrm{optical}}$ [26]. Furthermore, $\mathrm{NA} = 0.28$ is the numerical aperture of the microscope and $\lambda_{\mathrm{optical}} = 550\,\mathrm{nm}$ the wavelength of the scintillating light. The OTF correction is performed before phase retrieval by dividing the Fourier transform of the experimental images by the OTF. As discussed in the main text, the spread in energy deposition further degrades the transfer function of the scintillator, which explains the deviation of the reconstructed values from the expected phase shift of −0.8 rad. These findings emphasize the importance of correcting the indirect data for the total transfer function of the magnifying optics if aiming for a quantitative reconstruction. On the downside, noise is amplified by this correction as well.

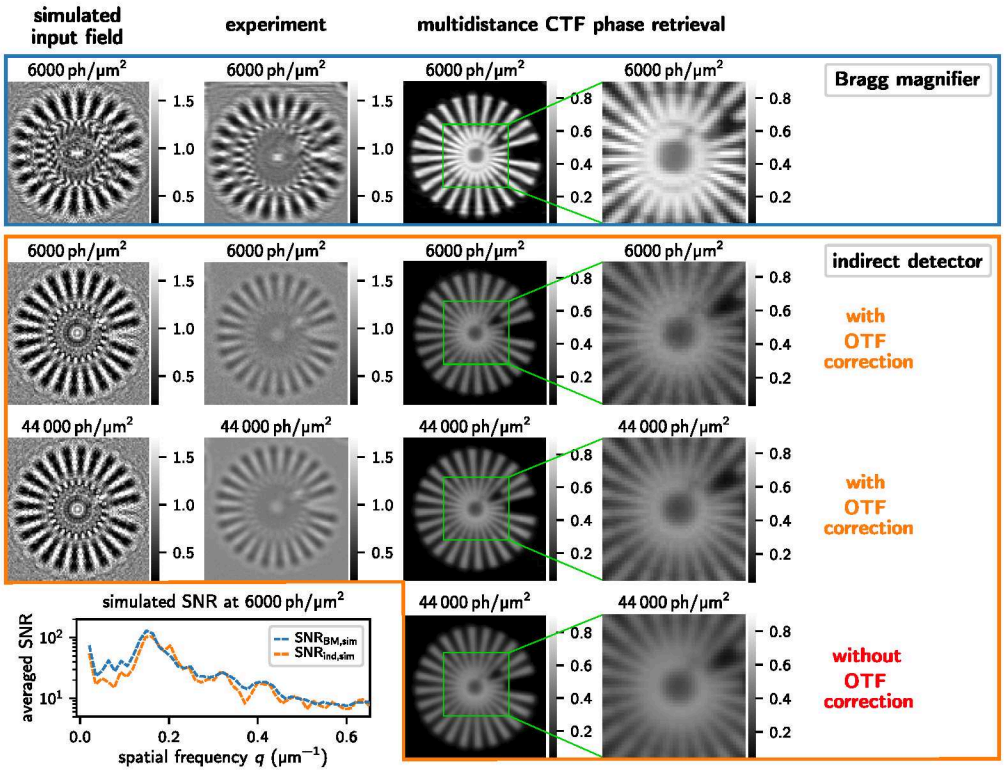


**Fig. S2.** Additional information for Fig. 3A in the main text. The first column shows simulations of the input wavefield and the second column depicts experimental data (after flat- and darkfield correction). The photon fluence is indicated in the caption of each image. The simulated and averaged SNR($q$) is shown in the graph in the last row. The propagation distances in the simulated and experimental holograms shown in the first two columns were $z = 41$ cm for the indirect system and $z_x = 41$ cm and $z_y = 79$ cm for the BM. The third column shows the multidistance phase reconstructions, with a zoom-in in the fourth column. In the second and third row, the indirect data have been corrected for the incoherent OTF of the microscope prior to phase retrieval, while the last row shows the result without OTF correction.

### B. Comparison between 12 µm thick LSO and 50 µm LuAG scintillator

Under the same conditions as in Fig. 3B, C in the main text, we measured also the SNR($q$) for a 50 µm thick LuAG scintillator, which has an overall X-ray absorption of nominally 35 % at 30.5 keV. Despite the higher absorption, the SNR at $q \approx 0$ is not increased. This might result from the lower light yield of LuAG (25 photons/keV [27]) and thus increased noise during optical conversion. Further, the SNR($q$) decreases faster with increasing $q$, as expected from the finite depth of field of the objective.

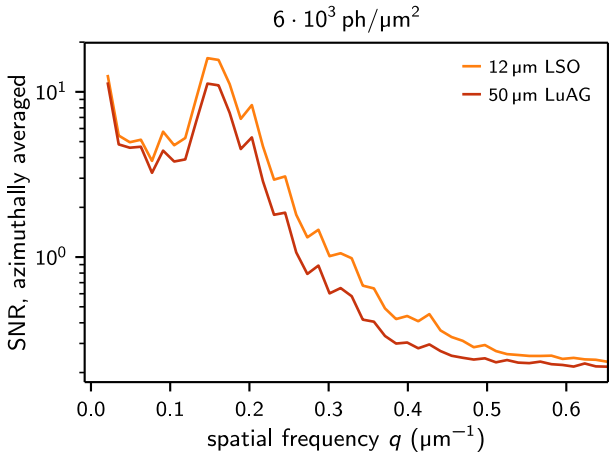


**Fig. S3.** Comparison between the 12 µm thick LSO scintillator and a 50 µm thick LuAG scintillator, measured under the same conditions as in Fig. 3B, C in the main text.

### C. Optimization of indirect system

The presented experimental comparison was performed for a specific spatial resolution of 1.6 µm, where both the indirect and the BM system have the same pixel size with respect to the sample. The question arises whether the parameters for the indirect detector, namely the NA, scintillator thickness and operating energy, can further be optimized and adjusted in dependence of the sample thickness and the desired resolution. The value to be maximized is the normalized $\mathrm{SNR}^2$ as shown in Fig. 1B in the main text. This optimization is a rather complex problem, for which we present an idealized upper estimate.

For each sample thickness, we calculate the theoretically achievable $\mathrm{SNR}^2$ over energy at constant dose, assuming a perfect detector, and find its maximum for the normalization (see green curves in Fig. 1B in the main text). Next, we compute the $\mathrm{SNR}^2$ that is maximally detectable by the indirect system at the desired spatial resolution. Varying the NA determines the allowed scintillator thickness. As a rule of thumb, the thickness $t$ can be chosen relative to the depth of field of the objective in the scintillator [28, 29]:

$$t \approx x \frac{\lambda_{\mathrm{vis}} \cdot n}{\mathrm{NA}^2},$$

where the refractive index $n = 1.82$ of the LSO scintillator is taken into account, and $x$ is typically chosen in the range of 1 to 2. Here, we show the results for $x = 2$. From the thickness, we can determine for each NA the $\mathrm{SNR}^2$ in dependence of the energy, where we also include the decrease by the OTF at the desired spatial resolution. For very low energies, we ensure that at least three optical photons are detected per absorbed X-ray photon in order not to degrade the X-ray statistics. The highest detectable $\mathrm{SNR}^2$ specifies the optimal NA and energy for each sample thickness and desired resolution. Division by the maximum of the theoretical $\mathrm{SNR}^2$ determines the normalized $\mathrm{SNR}^2$, i.e. the dose efficiency of the indirect system.

In Fig. S4A, we show the results of the optimization for different desired resolutions and sample thicknesses. For high resolution, the NA should be chosen rather high instead of optimizing the detection efficiency by increasing the scintillator thickness. This could be understood as follows: increasing the OTF contributes linearly to the SNR, while the scintillator absorption enters with the square root. In our experiment, it would probably have been beneficial to use a larger NA of 0.4 rather than increasing the scintillator thickness. This would have increased the OTF by a factor of 1.2 at $q = 0.3\,\mu\mathrm{m}^{-1}$ and a factor of 1.6 at the desired resolution $q = 0.6\,\mu\mathrm{m}^{-1}$. For lower resolutions, it is beneficial to decrease the NA in favor of a thicker scintillator and better X-ray statistics. The NA approaches a lower limit due to the collection efficiency of optical photons.

As mentioned in the main text, for thin samples ($< 5\,\mathrm{mm}$), the ideal operating energy for the indirect system would be 11 keV. Even for this case and a larger NA, the dose efficiency of the BM system would be one order of magnitude larger than for the indirect system at the desired resolution. For higher resolution, e.g. using Germanium crystals with 0.6 µm achievable resolution, the gain increases further, and liquid immersion would have to be used to reach such high NAs in the indirect system. As mentioned above, the efficiency calculated here is only an upper estimate, as we have also seen in our experiment. For example, the degradation of the OTF by generation of secondary particles in the scintillator is not included [30].

We performed the calculations for an LSO scintillator and a soft tissue sample. We uploaded the code in the Supplementary Material so that the interested reader can adapt the calculations for other sample materials and thicknesses, resolutions or scintillator materials.

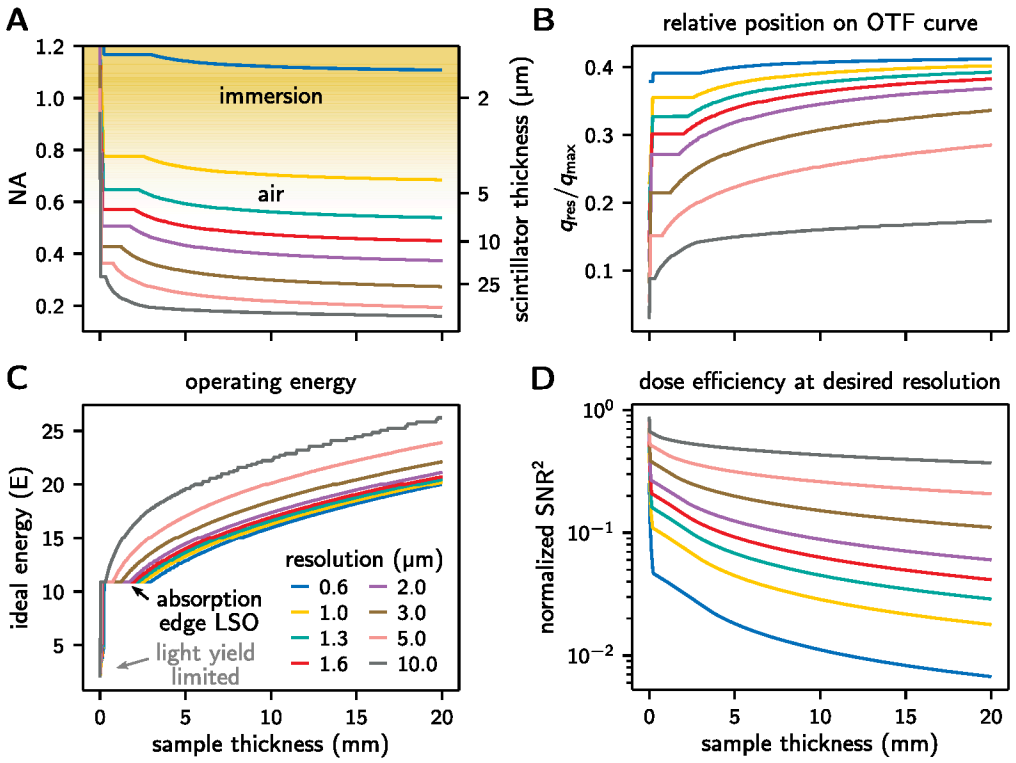


**Fig. S4.** Optimized parameters for the indirect system and an LSO scintillator for different sample thicknesses (material: soft tissue) and resolutions. **A** Optimized numerical aperture over sample thickness for different resolutions. We indicate that for high NA, objectives with immersion liquids are necessary. **B** Spatial frequency $q_{\mathrm{res}}$ that corresponds to the desired resolution in relation to the spatial frequency $q_{\mathrm{max}}$ where the OTF of the objective becomes zero. **C** Optimal operating energy. A lower limit is given by the light yield of the scintillator per absorbed X-ray photon (gray arrow). The absorption edge of LSO determines an optimal energy of 11 keV for thin samples (black arrow). **D** Resulting normalized SNR$^2$ at the desired resolution, which is an upper estimate for the dose efficiency compared to an ideal detector. The legend shown in C is valid for all panels.

## 6. MOTION ANALYSIS OF A *TRICHOGRAMMA CACOECIAE* WASP EMERGING FROM ITS HOST EGG

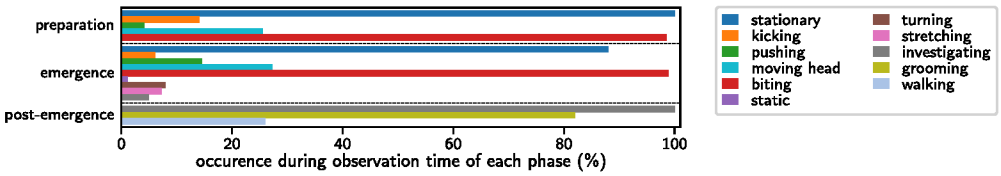


**Fig. S5.** Occurrence of movement patterns and behavioral acts observed in the emergence process of the *Trichogramma cacoeciae* wasp shown in Fig. 4B-D in the main text and Mov. S2. We assign the movement patterns and behavioral acts to three main phases: preparation, emergence, and post-emergence. In the preparation phase, the wasp moves its head continuously, accompanied by a high activity of the mandibles, and bites into the egg shell. Apparently, it performs coordinated movements of body, head, and mandibles in order to perforate the egg. We define the beginning of the actual emergence phase when the first body part (besides the mandibles) protrudes the egg shell, for this dataset at 00:42:41 h. During emergence, lasting 33 min here, the wasp tries to break through the egg shell by stretching its whole body several times, pushing its legs and continuously biting into the shell. When a contiguous hole is large enough, the wasp finally manages to emerge from the egg, after which the post-emergence phase begins. In this phase, the wasp grooms itself in vicinity of the egg and eventually departs. The observed durations are normalized to the total acquisition time of each phase (7.7 min, 21.3 min, 0.5 min). A description of the behaviors is given in the ethogram in Table S1.

## 7. ETHOGRAM OF A *TRICHOGRAMMA CACOECIAE* WASP EMERGING FROM ITS HOST EGG

**Table S1.** Description of behaviors observed in the emergence process of the *Trichogramma cacoeciae* wasp shown in Fig. 4B-D and Movie S2. Since the phase reconstructed radiographs are 2D projections of the laterally lying wasp, it is not possible to specify whether the wasp lays dorsally or ventrally towards the viewer. For each movement pattern and behavioral act, the total time of occurence is listed and the relative proportion compared to the overall length of the acquired image sequence (30 min) is mentioned. We would like to emphasize that the values should be regarded as estimate because the wasp was already active at the beginning of the recordings and radiation-free pauses were taken in between (see Section 1 - Materials and Methods).

| Movement pattern / behavioral act | Description | Total observed duration (min:ss) | Percentage (%) |
|---|---|---|---|
| Static | The wasp remains completely motionless | 00:14 | 0.8 |
| Stationary | The wasp does not change its body position along the anterior-posterior (AP) axis and no locomotion is carried out except of the head and legs | 26:29 | 89.7 |
| Turning | The wasp turns its whole body along the AP axis | 01:41 | 5.7 |
| Kicking | Moves legs uncoordinatedly | 02:23 | 8.1 |
| Pushing | Pushes legs against host egg shell | 00:25 | 11.6 |
| Stretching | Elongates its whole body along the AP axis by contracting its abdomen | 01:32 | 5.2 |
| Moving head | Turns, tilts, elongates or moves head in a pulling manner (excluding the head movement caused by using the mandibles) | 07:46 | 26.3 |
| Biting | Opens and closes its mandibles to cut a hole into the egg shell | 28:40 | 97.1 |
| Investigating | Moves antennae outside the host egg | 01:34 | 5.3 |
| Grooming | Cleans bodyparts using the legs and mouthparts | 00:25 | 1.4 |
| Walking | The wasp walks outside the host egg | 00:08 | 0.4 |

## 8. MOVIE CAPTIONS

**Movie S1** Flatfield-corrected projection images of a TEM gold grid measured with the BM system at different energies, showing variable magnifications. For details, see main text and Section 1 (Materials and Methods).

**Movie S2** *In vivo* movie of a *Trichogramma* wasp emerging from its host egg. As it was not possible to predict the time of emergence beforehand, the irradiation of the specimen was initially interrupted by several irradiation-free pauses in order to keep the overall dose at a minimum. In sequence 6 to 23, the setup experienced a slight drift, which was corrected after sequence 23 by realigning the pitch angle of the crystals. More details are given in the main text and in Section 1 (Materials and Methods). Please note that the time-varying 'cloudy' background pattern results from the amplification of low spatial frequency noise by phase retrieval [31, 32].

**Movie S3** *In vivo* movie of a *Trichogramma* wasp showing flexible movement of its mandibles. More details are given in the main text and in Section 1 (Materials and Methods).

## REFERENCES


1. D. Pennicard, S. Smoljanin, B. Struth, H. Hirsemann, A. Fauler, M. Fiederle, O. Tolbanov, A. Zarubin, A. Tyazhev, G. Shelkov *et al.*, "The LAMBDA photon-counting pixel detector and high-Z sensor development," J. Instrumentation **9**, C12026 (2014).
2. L. M. Lohse, A.-L. Robisch, M. Töpperwien, S. Maretzke, M. Krenkel, J. Hagemann, and T. Salditt, "A phase-retrieval toolbox for X-ray holography and tomography," J. Synchrotron Radiat. **27**, 852–859 (2020).
3. S. Hrivňak, J. Uličnỳ, and P. Vagovič, "Fast Fresnel propagation through a set of inclined reflecting planes applicable for X-ray imaging," Opt. Express **26**, 34569–34579 (2018).
4. P.-A. Douissard, A. Cecilia, T. Martin, V. Chevalier, M. Couchaud, T. Baumbach, K. Dupré, M. Kühbacher, and A. Rack, "A novel epitaxially grown LSO-based thin-film scintillator for micro-imaging using hard synchrotron radiation," J. Synchrotron Radiat. **17**, 571–583 (2010).
5. P.-A. Douissard, A. Cecilia, X. Rochet, X. Chapel, T. Martin, T. van de Kamp, L. Helfen, T. Baumbach, L. Luquot, X. Xiao *et al.*, "A versatile indirect detector design for hard X-ray microimaging," J. Instrumentation **7**, P09016 (2012).
6. M. Vogelgesang, T. Farago, T. F. Morgeneyer, L. Helfen, T. dos Santos Rolo, A. Myagotin, and T. Baumbach, "Real-time image-content-based beamline control for smart 4D X-ray imaging," J. Synchrotron Radiat. **23**, 1254–1263 (2016).
7. D. Paganin, S. C. Mayo, T. E. Gureyev, P. R. Miller, and S. W. Wilkins, "Simultaneous phase and amplitude extraction from a single defocused image of a homogeneous object," J. Microsc. **206**, 33–40 (2002).
8. T. Faragó, S. Gasilov, I. Emslie, M. Zuber, L. Helfen, M. Vogelgesang, and T. Baumbach, "Tofu: a fast, versatile and user-friendly image processing toolkit for computed tomography," J. Synchrotron Radiat. **29** (2022).
9. X. Yang, R. Hofmann, R. Dapp, T. van de Kamp, T. dos Santos Rolo, X. Xiao, J. Moosmann, J. Kashef, and R. Stotzka, "TV-based conjugate gradient method and discrete L-curve for few-view CT reconstruction of X-ray *in vivo* data," Opt. Express **23**, 5368–5387 (2015).
10. J. Dong, J. Fu, and Z. He, "A deep learning reconstruction framework for X-ray computed tomography with incomplete data," PLoS One **14**, e0224426 (2019).
11. A. Limaye, "Drishti: a volume exploration and presentation tool," in *Developments in X-ray Tomography VIII,* vol. 8506 (SPIE, 2012), pp. 191–199.
12. S. Huhn, L. M. Lohse, J. Lucht, and T. Salditt, "Fast algorithms for nonlinear and constrained phase retrieval in near-field X-ray holography based on Tikhonov regularization," Opt. Express **30**, 32871–32886 (2022).
13. J. B. Wolfgang Schlegel, *Medizinische Physik 2* (Springer, Berlin, Germany, 2002).
14. J. Allison, K. Amako, J. Apostolakis, P. Arce, M. Asai, T. Aso, E. Bagli, A. Bagulya, S. Banerjee, G. Barrand *et al.*, "Recent developments in Geant4," Nucl. Instruments Methods Phys. Res. Sect. A: Accel. Spectrometers, Detect. Assoc. Equip. **835**, 186–225 (2016).
15. T. Salditt, T. Aspelmeier, and S. Aeffner, *Biomedical Imaging* (De Gruyter, Berlin, Germany, 2017).
16. N. Hünemohr, H. Paganetti, S. Greilich, O. Jäkel, and J. Seco, "Tissue decomposition from dual energy ct data for mc based dose calculation in particle therapy," Med. physics **41**,

061714 (2014).
17. C. Homann, T. Hohage, J. Hagemann, A.-L. Robisch, and T. Salditt, "Validity of the empty-beam correction in near-field imaging," Phys. Rev. A **91**, 013821 (2015).
18. P. Modregger, D. Lübbert, P. Schäfer, R. Köhler, T. Weitkamp, M. Hanke, and T. Baumbach, "Fresnel diffraction in the case of an inclined image plane," Opt. Express **16**, 5141–5149 (2008).
19. A. Authier, *Dynamical theory of X-ray diffraction*, vol. 11 (Oxford University Press Inc., New York, United States, 2004).
20. J. B. Minkoff, S. K. Hilal, W. F. Konig, M. Arm, and L. B. Lambert, "Optical filtering to compensate for degradation of radiographic images produced by extended sources," Appl. Opt. **7**, 633–641 (1968).
21. G. A. Krusos, "Correction for X-ray source optical-transfer-function degradation of radiologic images by optical spatial filtering," in *Application of Optical Instrumentation in Medicine II*, vol. 43 (SPIE, 1974), pp. 63–74.
22. P. Cloetens, W. Ludwig, J. Baruchel, D. Van Dyck, J. Van Landuyt, J. Guigay, and M. Schlenker, "Holotomography: Quantitative phase tomography with micrometer resolution using hard synchrotron radiation X rays," Appl. Phys. Lett. **75**, 2912–2914 (1999).
23. P. Cloetens, "Contribution to phase contrast imaging, reconstruction and tomography with hard synchrotron radiation: principles, implementation and applications," Ph.D. thesis, Vrije Universiteit, Brussels (1999).
24. L. De Caro, F. Scattarella, S. Tangaro, D. Pelliccia, C. Giannini, U. Bottigli, and R. Bellotti, "Deconvolution by finite-size-source effects of X-ray phase-contrast images," Med. Phys. **38**, 1951–1961 (2011).
25. Y. Wang, G. Li, J. Zhang, Q. Yi, Y. Zhao, K. Li, Y. Zhu, and X. Jiang, "Improving the detection efficiency and modulation transfer function of lens-coupled indirect X-ray imaging detectors based on point spread functions simulated according to lens performance parameters," J. Synchrotron Radiat. **25**, 1093–1105 (2018).
26. J. W. Goodman, *Introduction to Fourier optics* (Roberts and Company publishers, Englewood, Colorado, United States, 2005).
27. crytur, "LuAG:Ce," (2023). [https://www.crytur.com/materials/luagce; accessed 7. Oct. 2023].
28. X. Chen, L. Ren, Y. Qiu, and H. Liu, "New method for determining the depth of field of microscope systems," Appl. Opt. **50**, 5524–5533 (2011).
29. M. Born and E. Wolf, *Principles of optics: electromagnetic theory of propagation, interference and diffraction of light* (Elsevier, 2013).
30. L. Wollesen, F. Riva, P.-A. Douissard, K. Pauwels, T. Martin, and C. Dujardin, "Scintillating thin film design for ultimate high resolution X-ray imaging," J. Mater. Chem. C **10**, 9257–9265 (2022).
31. D. Paganin, A. Barty, P. J. McMahon, and K. A. Nugent, "Quantitative phase-amplitude microscopy. III. The effects of noise," J. Microsc. **214**, 51–61 (2004).
32. Y. Zharov, E. Ametova, R. Spiecker, T. Baumbach, G. Burca, and V. Heuveline, "Shot noise reduction in radiographic and tomographic multi-channel imaging with self-supervised deep learning," Opt. Express **31**, 26226–26244 (2023).